Hydraulic failure of granular materials with artificial cementation

Abbas Farhat,* Pierre Philippe,† Li-Hua Luu, and Alexis Doghmane
RECOVER, INRAE, Aix Marseille Univ, 3275 route de Cézanne, 13100 Aix-en-Provence, France

Pablo Cuéllar
BAM, Federal Institute for Materials Research and Testing, Division 7.2 for Buildings and Structures, Unter den Eichen 78, 12205 Berlin, Germany

(Received 24 October 2023; accepted 7 June 2024; published 24 June 2024)

This paper presents an experimental study on the hydraulic failure of a submerged layer of cemented soil stressed by a localized upward water flow. Different mixtures of glass beads bonded with solid paraffin bridges were used as artificial material for the cemented granular soil. Variations in the cementation strength of the material were carefully introduced with different particle sizes and binder contents. The hydraulic fracture tests were then carried out with an upward flow injected at a controlled rate through a small section at the bottom of the samples. From a phenomenological perspective, the results reveal the existence of at least three modes of failure for a cemented soil layer: (1) overall block uplift, (2) block rupture by median crack at the inflow zone, and (3) progressive excavation of a fluidized path along the walls. The critical flow rate and pressure drop conditions at failure have been carefully quantified for the different mixtures and layer thicknesses, leading to a fair estimation of the hydraulic resistance of the samples, which here is found to be virtually independent of the grain size. However, the test results also showed inconsistent failure modes precluding so far the derivation of a simple phase diagram. Nevertheless, it was possible to rationalize all the measured data by employing appropriate modifications of the classical dimensionless numbers that describe the fluidization of purely frictional materials, whereby the cementation strength of the soil is quantified at the microscale through the yield tensile force of the intergranular bonds. Irrespective of its subsequent development, during which boundary conditions obviously play a major role, the initiation of the instability appears to take place very locally at the inlet when the drag force induced by the flow overcomes the cementation strength of the paraffin bonds. The results of this study thus appear to endorse the extension of the dimensional relationships of particulate systems in interaction with fluid flows to the case of cemented granular materials, in a similar vein as in recent previous studies.

DOI: 10.1103/PhysRevFluids.9.064305

I. INTRODUCTION

Cementation in a granular soil usually takes place as the partial filling of the pore space between grains by a solid binder that connects the grains and generally stiffens the material. Its origin can be natural, and it is encountered in a large number of geological formations, often in steep cliffs, involving several types of cemented soils, such as breccias, carbonate sands, or sandstones [1,2]. Precipitation and deposition of mineral constituents, such as carbonates, is the main origin

*Contact author: abbas.farhat@inrae.fr
†Contact author: pierre.philippe@inrae.fr

of the common natural soil cementation, but some biological binders also exist, due to organic (bacterial, microbial) sources [3,4]. Reproducing artificially these natural processes is of great practical interest and has long been used in the construction industry with various types of cement [2]. This cementation process can also be used to reinforce existing soils [3–5] and is motivating a growing number of studies in view of the expected benefits in terms of sustainable development or reduced environmental and energy impact [6,7]. Soils treated by artificial cementation gain in strength and generally become far more rigid, but also become sensitive to local fracturing and further cracks development on a larger scale under sufficient stress [8].

The resistance of these natural or artificial cemented soils specifically to hydraulic loading is an important issue, sandstone being, for instance, very common in deep seabeds, creating a growing interest from the offshore community [9]. A particular and critical situation is that of a focused flow through a cemented soil. Such hydraulic configuration can be encountered in the presence of a leak in a pipe or when a preferential seepage path is created in the foundation of a hydraulic structure.

The latter scenario may actually take place during the initiation phase of an internal erosion mechanism, known as backward erosion piping [10], which is a frequent threat to fluvial or coastal levees built on alluvial basins. This major risk has therefore been the focus of a great deal of research and development work over the years, from the analytical, numerical, and experimental points of view, and at various scales, from the laboratory to the field [11,12]. The erosion mechanism is locally initiated by entrainment of soil at the surface of the downstream layer, at the embankment toe, under the effect of preferential flow under the structure, generally along existing structural weaknesses. Localized fluidization [13], also described as sandboil [14], or uplift is thus observed, depending on whether the soil is granular or cohesive. The subsequent development of the process involves enlargement of the initial eroded cavity, backward expansion along pipes, and, potentially, ultimate rupture of the structure [10]. Strengthening of the downstream cover layer can be used as preventive measure against backward erosion piping, for instance, by inserting a coarse sand barrier [15,16]. The inherent or induced cohesion within this cover layer may also govern the critical stress threshold for the onset of backward erosion piping and will be the subject of this study in the specific case of solid cohesion, i.e., for cemented soils introduced earlier.

More broadly in terms of applications, we present here an investigation of the failure of a cemented granular soil when subjected to localized upward hydraulic flow, a study that can be viewed as an extension of several previous experimental and numerical works on the localized fluidization of purely frictional soils (i.e., soils with zero tensile resistance) where a fluidized cavity expands upward to create a steady vertical chimney [13,17–21].

Reviewing the related literature, only very few studies have addressed such topics to some extent. Using the same configuration, but with hydraulic flow in the other direction, i.e., downward infiltration flow, some of the present authors have carried out experiments [22]. Other than this, a few numerical studies can also be mentioned, all based on similar approaches coupling lattice Boltzmann and discrete elements methods in two dimensions, with the addition of an adhesive contact model between neighboring grains. The reader may refer, for instance, to [23,24] and references therein for more information on the numerical methods and other examples of soil erosion applications. More specifically, as far as the present localized hydraulic failure situation is concerned, Cui and coauthors [25] investigated exactly the present configuration and mostly qualitatively showed that an increasing adhesion force between particles generates less dilation in the bed, with progressive appearance of cracks during cavity expansion from the inlet. Using a backward erosion piping, with a uniform outflow and specific boundary conditions to impose the location of the eroded zone, Tran and coauthors [26] proved the method's ability to reproduce this particular type of erosion, but on a single set of parameters. The same kind of situation was simulated also in [22] and confirmed two scenarios for the rain-induced formation of sinkholes: dropout and subsidence. The intention of this paper is to fill the gap and supplement the scarce insights available in the literature with proper physical experiments and a systematic approach.

Another point of clarification concerns the type of cemented materials considered in this paper. These involve coarse grains interconnected at contacts by solid bonds, assuming that the solid binder

is almost exclusively present in the adhesive bridges and not distributed on the particle surface as a coating [27]. This experimental study is based on the preparation of such artificial cemented granular materials, made of glass beads bonded by paraffin bridges, whose cementation strength has been quantified at both contact and sample scales in previous works by the authors [28,29]. In particular, we propose to consider the microscopic yield tensile resistance of a single bond, for which an analytical expression has been derived and reads [29]

$$F_t = 1.80\sigma_{gp}\sqrt{\frac{\xi_p}{Z}}d^2, \tag{1}$$

where σ_{gp} denotes the intrinsic adhesive strength at contact between glass and solid paraffin, Z is the mean coordination number within the cemented sample, d is the grain diameter (supposed here identical for the two bonded particles), and ξ_p is the volume fraction in paraffin used to prepare the sample. Assuming $Z = 8$, a satisfactory fit to the experimental data provided $\sigma_{gp} \approx 0.275\,\text{MPa}$ [29]. This final expression for F_t conveniently allows the cementation strength of the material to be precisely adjusted, according to the size of the glass beads and the amount of paraffin in the solid bridges, and to be used as a control parameter in the following.

A relevant dimensionless group for these granular systems with interparticle adhesion is the so-called cohesive granular Bond number, denoted Bo_g, which compares gravitational (and frictional) effects with cohesion [8,30–32]. Defined at the microscopic scale, and including buoyancy, this dimensionless number can be written as [24,33]

$$\text{Bo}_g = \frac{F_t}{(\rho_g - \rho_f)gd^3}, \tag{2}$$

with ρ_g and ρ_f the density of grains and surrounding fluid, respectively. Note that this expression differs from a numerical prefactor when defined at the macroscopic scale using an homogenized tensile stress [29,34].

The remainder of this article is organized as follows: Sec. II describes the artificial material used as a cemented granular soil as well as the experimental setup developed to study localized hydraulic failure of this material, with all related technical details. The results obtained in the physical tests are then presented in Sec. III, starting with the observed phenomenology of hydraulic failure, which reveals three different scenarios, then presenting the evolution of hydraulic quantities during a test and the determination of critical conditions. Section IV then analyzes these critical values, focusing specifically on dimensionless numbers to rationalize the results. To conclude, a final summary is then provided in Sec. V.

II. EXPERIMENTAL DEVICES

The aim of our experiments is to test the resistance and destabilization scenarios of a cemented granular soil layer subjected to upward liquid flow from a restricted injection zone at its base. In this section, we present the different materials used, as well as the experimental device developed and its protocol.

A. Materials and sample preparation

Here we briefly describe the artificial material used in our experiments and its preparation; further details can be found in a recent article dedicated to the micro- and macro-mechanical characterization of these cemented granular materials [29]. To artificially prepare a bridge-cemented granular material, it is necessary to select grains and a solid binder that can be localized only at the points of contact between grains. We used here three sets of almost monosize glass beads with diameter $d = 0.70 \pm 0.15\,\text{mm}$, $d = 1.40 \pm 0.15\,\text{mm}$, and $d = 3.0 \pm 0.3\,\text{mm}$, respectively. These beads, supplied by Sigmund-Lindner GmbH, are made of silicate glass with density $\rho_g = 2650\,\text{kg m}^{-3}$ and have a polished surface finish. Paraffin wax was chosen as the binder for a number of practical

reasons. First, it is easy to melt and mix with the beads. Second, liquid paraffin wets the glass poorly, causing the liquid phase not to cover the surface of the beads, but to form capillary bridges between them, where it concentrates almost exclusively. Finally, the reduction in volume of these bridges during cooling is rather limited, estimated at 10%, which reduces the risk of degradation of the final solid adhesive contact [33]. The commercial paraffin used here was supplied by Chimie-Plus Laboratoires; its solid density and melting temperature are approximately 880 kg m^{-3} and 50 °C, respectively.

After weighing the masses of beads and solid paraffin for the target mass fraction X_p, or equivalently volume fraction $\xi_p = X_p\rho_g/\rho_p$, paraffin is first melted alone and then gently mixed to distribute the liquid phase evenly among the beads. Right after that, the hot mixture can be deposited in the cell following a precise protocol described below and left for at least 7 hr until complete hardening of the paraffin bridges. The layer of bonded grains thus created can then be immersed in a liquid.

The liquid chosen for these experiments is not pure water, but rather a more viscous liquid, in order to generate sufficient stress in the material while maintaining an almost laminar flow in the porous layer. The liquid selected for this study was a mixture composed of 65% of glycerol and 35% of distilled water, with a density $\rho_l = 1180$ kg m^{-3} and a viscosity $\mu_l \approx 24$ cP at 22 °C (measured with a ball viscometer). As shown below, this choice leads to porous Reynolds numbers below 150 in all our tests, that is, flows just up to the transition from laminar to turbulent porous regime [35].

B. Description of the experimental device and procedure

After several stages of development, the final version of the device is pictured in Fig. 1. It consists of a central cell box mounted on a vertical support, made up of a metal frame with removable lateral windows in plexiglass, whose internal dimensions are $h = 30$ cm in height, $w = 20$ cm in width, and $l = 10$ cm in depth. The cell is connected to inlet and outlet pipes at its base and top through valves featuring absolute pressure sensors (model dTRANS p30 provided by Jumo, 1 kPa accuracy). The hydraulic circuit is arranged in a closed loop including a liquid buffer tank, where the flow is induced by a gear pump (model GG 419 supplied by Viking) with rate control by a precalibrated frequency driver, with a maximum capacity of 32 l min^{-1}.

The granular layer is then arranged into the cell, not directly on the cell bottom but on an inserted plate. The hot mixture of beads and liquid paraffin is poured by gravity through a funnel maintaining approximately a constant drop height of few centimeters. The height H of the sample can be varied, and the solid volume fraction ϕ of the packing thus created has been estimated at 0.61. Following initial preliminary tests and as discussed later in Sec. III A 3, we have added to the sample construction a preliminary phase of paraffin coating on the bottom plate and on the side walls (to a height of H). This superficial treatment is carried out before the cell is assembled, side by side and horizontally, using hot liquid paraffin, which is then left to cool down and harden. This step substantially strengthens the attachment between the cemented layer and the cell at the boundaries.

The plate supporting the sample was specifically designed and fabricated by 3D printing. The plate is fitted with a groove and an O ring on its 1 cm thick side edge to seal it hydraulically at the contact with the lateral walls. The plate is stiffened and vertically supported with six egs to ensure a firm fixation to the base of the cell and to avoid plate deformations that could induce fractures in the sample. The plate features at its center a circular cut with $D_i = 25$ mm in diameter with a grid at its top to retain the beads over the plate and where the cylindrical inlet pipe is attached. The discontinuous inlet pipe focusing the fluid flow from the base of the cell up to the injection point at the bottom of the cemented layer is arranged with a small (1 cm) gap between its upper and lower sections, which permits the successive saturation of the different cell chambers using the same liquid inlet (i.e., first the chamber below the plate, then the porous cemented layer, and then the rest of the upper chamber). The fluid introduction and saturation stage is carefully performed with very low flow rates to optimize air removal and minimize the bubble retention.

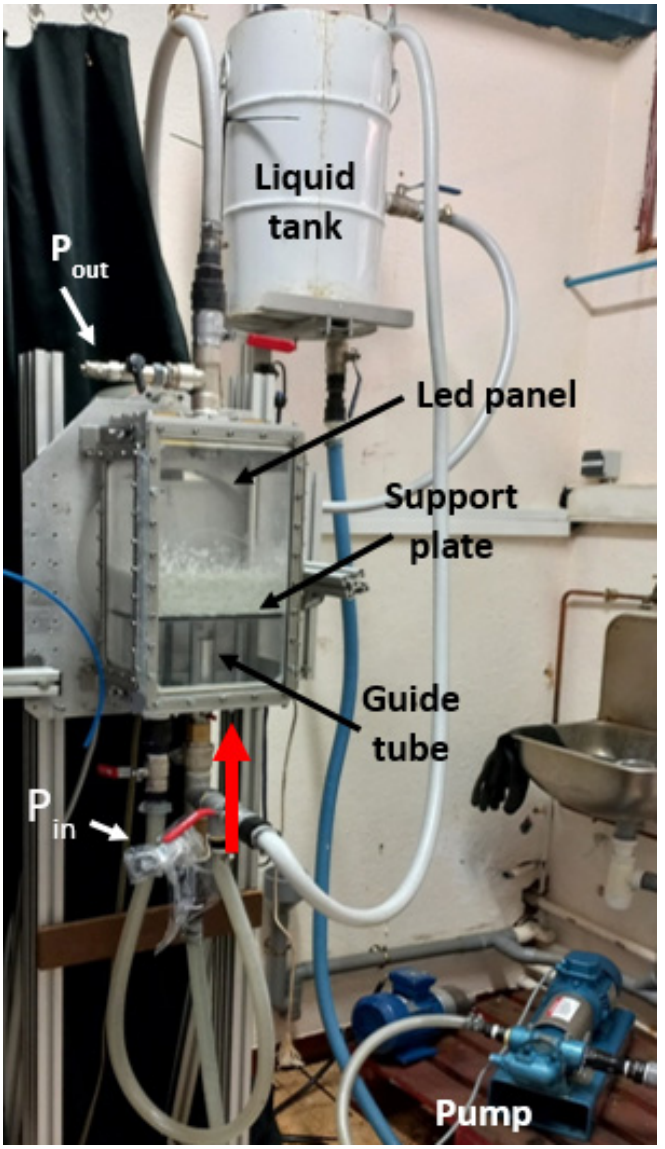

FIG. 1. Picture of the experimental device.

Visualization of the sample and monitoring of its evolution over time are carried out by backlighting and image acquisition with a digital camera (model XiQ MQ042MG-CM by Ximea) placed on a tripod in front of the cell. An LED panel (model 1800 Lumen supplied by Inspire Gdansk) is placed at the back of the sample so that the variations in transmitted light intensity provide an indication of mass grain movement or fracture development. Image resolution is approximately 10 pixels per millimeter.

Each test is carried out by progressively increasing the injection rate. Inlet and outlet pressures, denoted P_{in} and P_{out} respectively, are monitored at a frequency of 5 Hz, while the image sequence is recorded at 25 frames per second. The test is stopped when a failure event is observed and has sufficiently developed. The hydraulic quantities of interest are the flow rate Q imposed by the pump and the pressure drop, $\Delta P = P_{\text{in}} - P_{\text{out}}$, induced by the flow passing through the sample of height H.

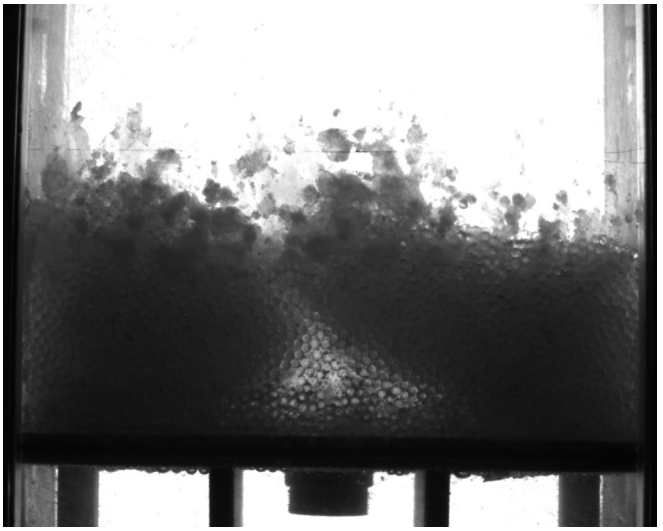

FIG. 2. Example of block rupture for $d = 3.0\,\text{mm}$, $X_p = 0.2\%$, and $H = 5\,\text{cm}$.

III. EXPERIMENTAL RESULTS

In this section we first present the general phenomenology observed during hydraulic failure tests, followed by the results obtained from a more systematic quantitative study of critical failure conditions as a function of the various material control parameters: grain diameter, paraffin content, and height of the cemented layer.

A. Phenomenology

During the physical tests, the flow rate through the injection at the bottom of the sample is increased manually, generally in regular increments every 20 sec. The sample initially remains perfectly static, with the differential pressure ΔP generated by the flow in the porous layer increasing in proportion to the flow rate Q. Then, beyond a certain threshold, the cemented grains can no longer withstand the percolating flow, leading to sample failure in one of the following modes (three different modes observed so far): either a median rupture into two blocks, a progressive burrowing of a fluidized path, or as a block uplift. These three scenarios of destabilization by localized hydraulic thrust are described below.

1. Block rupture

Block rupture, illustrated in Fig. 2, takes place as a local breakage of cemented bonds that remains spatially limited to the zone directly underneath the flow inlet.

This failure mode generally features a vertical fracture in the cemented layer, separating it into two blocks. A roughly triangular cavity appears then beneath these two blocks, which are partially lifted by the flow, while only a minor degradation of the bonded grains in contact with the corners of the walls takes place. The fracture generally occurs very suddenly, with no prior movement recorded by the camera. The appearance of the fracture leads then to a gradual decrease in the hydraulic pressure difference, as shown in Fig. 3.

2. Fluidized path

The second type of failure is the development of a fluidized path along the walls, between the sample and the cell, as shown in Fig. 4, where the sample has the same bead diameter but a lower

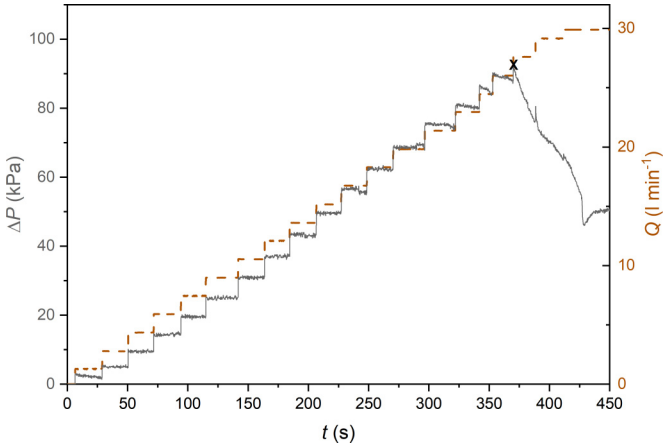

FIG. 3. Temporal evolution of the hydraulic pressure difference and the flow rate for the block rupture displayed in Fig. 2. The black cross indicates failure onset.

paraffin content than the one used for the previous block rupture in Fig. 2. Figure 5 presents the differential pressure measured during the test of Fig. 4 and is representative of the general fluidized path behavior.

This failure mechanism is clearly more gradual than the block rupture, taking place over at least two successive flow stages such as in the present case. Furthermore, for equivalent flow rate ranges, the pressure remains lower at the moment of rupture (probably due to the lower paraffin content in this test), and its subsequent pressure drop is very limited. The differential pressure then follows the successive increases in flow rate, but with no new drop, indicating that the path has stabilized and that there is no further substantial bond breakage and grain erosion (as confirmed by the images).

3. Block uplift

The last scenario observed for hydraulic failure is block uplift that corresponds to the detachment of the entire sample from the cell and its subsequent upward mobilization by the flow, as illustrated

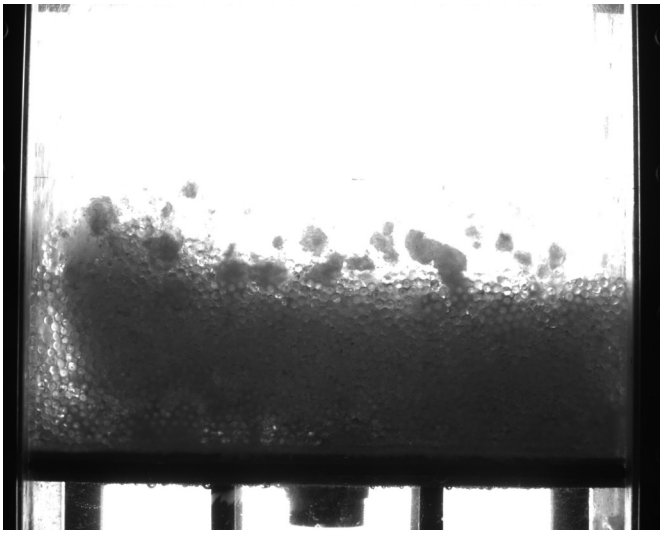

FIG. 4. Example of a fluidized path (at the left side wall) for $d = 3.0\,\text{mm}$, $X_p = 0.1\%$, and $H = 5\,\text{cm}$.

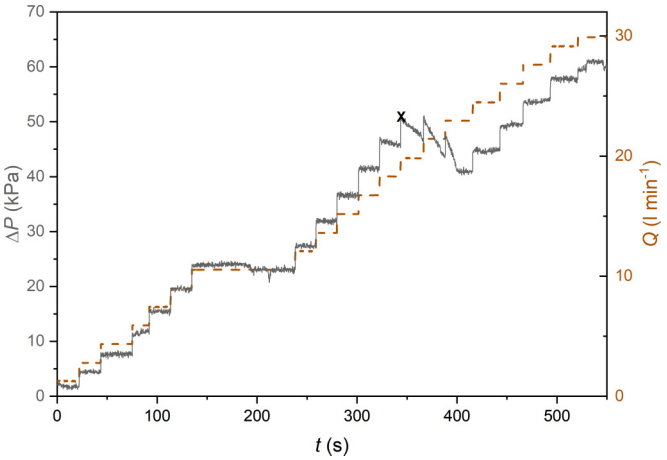

FIG. 5. Temporal evolution of the hydraulic pressure difference and flow rate for the fluidized path failure mode displayed in Fig. 4. The black cross indicates failure onset.

in Fig. 6, where the sample has the same paraffin content but a smaller bead diameter as for the case in Fig. 4.

This type of failure was in principle unexpected as it requires the rupture of all adhesive bridges at the sample boundaries, i.e., the side walls and the bottom plate. Because the drag force induced by the flow on the entire block is greater than its buoyant weight, the block then takes off as a whole just after wall debonding to reach a certain equilibrium height. The typical pressure evolution during a block uplift test is shown in Fig. 7.

As in the other cases, the differential pressure at first follows almost linearly the increase in flow rate at each increment, being essentially constant until the next increment. However, above a certain flow rate, the pressure fails to remain stable but decreases over the course of the stage, which appears to signalize the degradation at the sample boundaries leading to one or more preferential flow paths. The block uplift is then triggered suddenly at the next increment, creating an instantaneous drop in

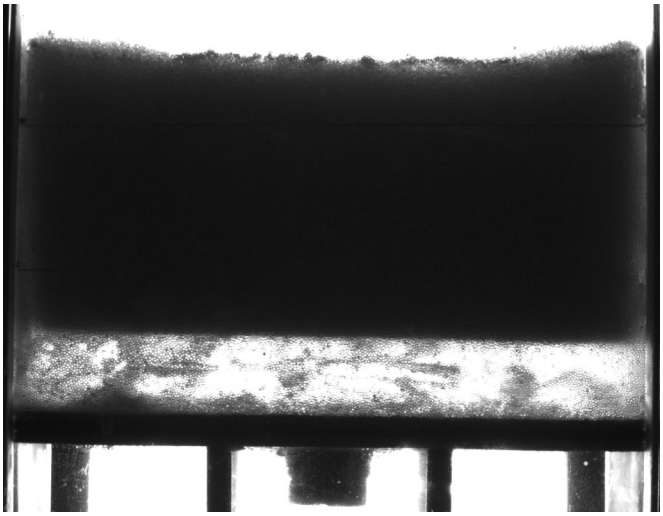

FIG. 6. Example of block uplift for $d = 0.7\,\text{mm}$, $X_p = 0.1\%$, and $H = 8\,\text{cm}$.

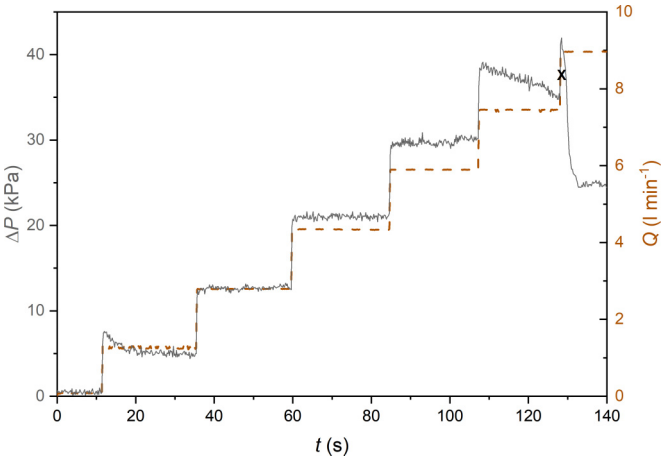

FIG. 7. Temporal evolution of the hydraulic pressure difference and flow rate during the block uplift displayed in Fig. 6. The black cross indicates failure onset.

differential pressure which eventually stabilizes when the block finds a position of equilibrium after having been dragged upwards for a few centimeters by the flow.

This behavior appears to indicate the weakness of the cemented layer at its boundaries likely due to the fact that the confining walls are flat. This condition constrains the arrangement of the grains touching the wall while reducing their coordination number. As a result, there is more pore space for flow along the walls, which can locally increase the hydraulic stress while the number of solid bridges is lower (lower coordination number). This type of destabilization also reflects the strong influence of the boundary conditions in this setup and is therefore less relevant from an application point of view. Since the block uplift was observed almost systematically in the first experiments we carried out, we decided for subsequent tests to use the wall precoating technique described in Sec. II B. This treatment makes the solid bridges in contact between the sample and the walls larger and stronger, thus inhibiting the initiation of block uplift to some extent. Nevertheless, and despite this reinforcement at the boundaries, several instances of block uplift failure still took place for setup configurations involving thicker samples (the case of Fig. 6) or higher paraffin contents.

As a complement to the block uplift description, we can analyze in greater detail the only two experiments carried out without wall precoating (and not listed in the forthcoming Table I) that ended up with this type of failure. The samples are 5 cm high and contain 0.2% paraffin by mass, with 1.4 mm beads in one case and 3 mm beads in the other. The maximal pressure difference measured just before subsequent drop due to uplift is 20.6 kPa and 18.8 kPa, respectively. These values can be compared with a simple analytical estimation. First, we can roughly estimate the number of solid bridges that need to be broken by asuming N_l particles in contact and bonded with the four side walls, which would be detached by bond shearing, and N_b particles in contact with the base, which would be detached by bond traction. The force F_t required for tensile adhesive debonding is quantified in Eq. (1). With regard to shear debonding, the authors showed that the corresponding critical force was generally proportional to F_t, with a coefficient C_s found to be of the order of 0.4 [29]. As a first approximation, the number of particles in contact with a wall is roughly deduced from the bulk volume fraction ϕ. Then the overall force required to break all the grains at the boundaries is given by

$$F = (N_b + N_l C_s)F_t = \frac{4\phi}{\pi d^2} S_b \left(1 + C_s \frac{S_l}{S_b}\right) F_t, \tag{3}$$

where $S_l = 2(l + w)H$ and $S_b = lw$ are the lateral and bottom areas, respectively.

TABLE I. Parameters of the experiments with wall precoating. Critical values for flow rate Q_c and pressure drop ΔP_c at failure, the type of which is indicated by R (block rupture), F (fluidized path), or U (block uplift).

Bead diameter d (mm)	Paraffin mass content X_p (%)	Layer height H (cm)	Critical flow rate Q_c (l min^{-1})	Critical pressure drop ΔP_c (kPa)
0.7	0.05	5	1.57 ± 0.01	4.9 ± 0.5 (R)
0.7	0.1	5	4.36 ± 0.01	18.5 ± 0.3 (F)
0.7	0.1	8	8.96 ± 0.01	41.5 ± 0.5 (U)
0.7	0.7	5	12.2 ± 0.4	53.3 ± 1.2 (U)
1.4	0.05	5	7.42 ± 0.02	23.8 ± 0.7 (F)
1.4	0.1	5	13.75 ± 0.01	45.9 ± 1.1 (R)
1.4	0.2	5	16.1 ± 0.1	51.6 ± 0.9 (R)
1.4	0.7	5	27.60 ± 0.01	96.8 ± 1.0 (U)
3.0	0.033	5	10.53 ± 0.01	49.1 ± 1.2 (R)
3.0	0.033	5	13.61 ± 0.01	51.6 ± 0.9 (R)
3.0	0.1	5	19.81 ± 0.02	50.2 ± 0.5 (F)
3.0	0.2	5	26.02 ± 0.01	89.0 ± 0.6 (R)

By substantial simplification, from this force F to be induced by the flow through the cemented granular layer, we can derive an approximate pressure drop $\Delta P = F/S_b$, which should provide a relevant order of magnitude for the critical differential pressure ΔP_c required for destabilization by block uplift. Note that the expression obtained for F, or equivalently ΔPc, is completely independent of grain size, since the microscopic adhesive force F_t is proportional to d^2. This is consistent with the two relatively close values obtained for ΔP_c in the experiments. In the end, the analytical expression provides $\Delta P_c \approx 17$ kPa, which is slightly smaller, but in reasonable agreement with the experimental data.

In summary, this complete phenomenology presents failure modes that are difficult to predict beforehand, and strongly conditioned by the boundary conditions of the system. A more comprehensive study is presented in the following section in an attempt to better rationalize this complex behavior.

B. Parametric study results

Following the same approach as in several previous experimental studies of localized fluidization in granular materials [13,17,19,21], we have carried out systematic measurements of the critical thresholds for hydraulic failure, in terms of flow rate Q_c and differential pressure ΔP_c, as a function of the sample control parameters grain size and layer height, supplemented here by the tensile strength of the intergranular cementation bonds. In practical terms, we carried out 12 tests with the wall precoating procedure, whereby each test took at least 2 days to complete. As presented in Table I, the parameter range explored here includes bead diameters of 0.7, 1.4, and 3 mm, paraffin mass contents from 0.033 to 0.7%, and sample bed heights of 5 and 8 cm.

Error bars in Table I are estimated as follows. In almost all cases, the decrease in pressure difference ΔP is clearly distinguishable during a given stage at imposed flow rate, often at the very beginning or after a short period. The critical flow rate Q_c is therefore perfectly known, while the critical pressure drop ΔP_c is determined by averaging, with an uncertainty linked solely to fluctuations. In the few cases where there is doubt about the critical level, the flow and pressure values are averaged over the corresponding range, with the standard deviation as range of uncertainty. In the end, these error bars remain very limited (even almost negligible for Q_c). Consequently, they will mostly not be visible on the graphs presented below since they are smaller or of the same order of magnitude as the size of the symbols used.

Figure 8 shows the pressure difference ΔP as a function of the imposed flow Q for the different experiments carried out with 0.7, 1.4, and 3 mm beads, respectively (see Table I).

In all cases, we initially observe a roughly linear relationship between the two quantities. The appearance of one of the three types of hydraulic failure, as described above, induces a more or less marked pressure drop. The critical conditions of rupture in terms of differential pressure ΔP_c and flow rate Q_c measured at the moment of failure are reported in Table I.

For the largest bead size tested here, namely, for $d = 3.0$ mm, there were no block uplift events observed [see Fig. 8(c)] but rather block ruptures. However, Figs. 8(a) and 8(b) show that for the smaller bead diameters, block uplift failures took place consistently with the highest critical values, in configurations with either the greatest sample height or for the highest paraffin contents.

The distinction between fluidized path and block rupture as a function of the critical values of ΔP_c or Q_c is, however, not obvious, with clearly different evolutions on each of the three graphs. From least to most resistant (i.e. according to critical values), the 0.7 mm samples successively failed by block rupture, fluidized path, and then block uplift. In contrast, for the 1.4 mm bead samples, the fluidized path is observed first, followed by block rupture before block uplift. Finally, in the case of the 3 mm samples, the fluidized path is only an intermediate case among the three block ruptures observed.

For the only test where the height of the sample was modified (from 5 to 8 cm otherwise featuring $d = 0.7$ mm and $X_p = 0.1\%$), we observe, as expected, an increase in failure thresholds for the thicker cemented layer. Finally, we can also note that the two repetition tests (namely, with $d = 3.0$ mm, $X_p = 0.033\%$) are reasonably similar in terms of the same failure mode and almost the same critical pressure drop, appearing to indicate a satisfactory repeatability of the tests.

All in all, the proposal of a simple phase diagram does not appear possible or pertinent so far due to the reduced exploration area imposed by technical limitations and the lack of a clear distinction between the different modes of failure.

IV. RESULTS ANALYSIS

A. Hydraulic resistance before failure

Before getting into the analysis of the critical values for failure triggering, it is worth examining the initial phase corresponding to the flow through a static porous medium. In the Darcy regime, a linear relationship between head loss and flow is expected. This is absolutely the case for 0.7 mm samples [see Fig. 8(a)], but deviations from a linear relationship are apparent for $d = 1.4$ mm [Fig. 8(b)] and even more so for $d = 3$ mm [Fig. 8(c)]. This can be explained by the fact that, as the diameter increases, the flow departs from the Darcy regime towards higher Reynolds numbers, with the appearance of inertial effects. For Reynolds numbers higher than 10, the addition of a quadratic term is commonly proposed to account for this effect in the pressure-flow relationship; see, e.g., Ergun's law or equivalent [35,36]. Considering the hydrodynamic regime at the entrance to the porous medium, the range explored by the porous Reynolds number at the injection point Re_i, i.e., considering the grain diameter d and the cross-sectional inflow into the bed $\frac{4Q}{\pi D_i^2}$ as typical velocity, goes up to 16, 64, and 146 for the 0.7 mm, 1.4 mm, and 3 mm bead samples, respectively. This confirms that the Darcy regime is gradually being lost as the beads increase in diameter.

However, since the deviation from the linear case remains reasonably limited, it is possible to approximate the value of the hydraulic resistance R_h from the critical values, that is, $R_h = \frac{\Delta P_c}{Q_c}$. This hydraulic resistance depends on the intrinsic permeability k of the porous medium, but also on the flow configuration, which in this case is a divergent flow from a rather small injection. As shown in Fig. 9, the values obtained for R_h vary very little, fluctuating around 2×10^8 kg m^{-4} s^{-1}, even though the bead diameter increases by more than a factor of 4. It is worth noting the wide dispersion observed for the largest beads [also pointed out by the lack of overlap of the curves in Fig. 8(c)], as well as the consistently higher resistance value when the height of the sample increases from 5 cm (solid symbol) to 8 cm (hollow symbol) for $d = 0.7$ mm and $X_p = 0.1\%$.

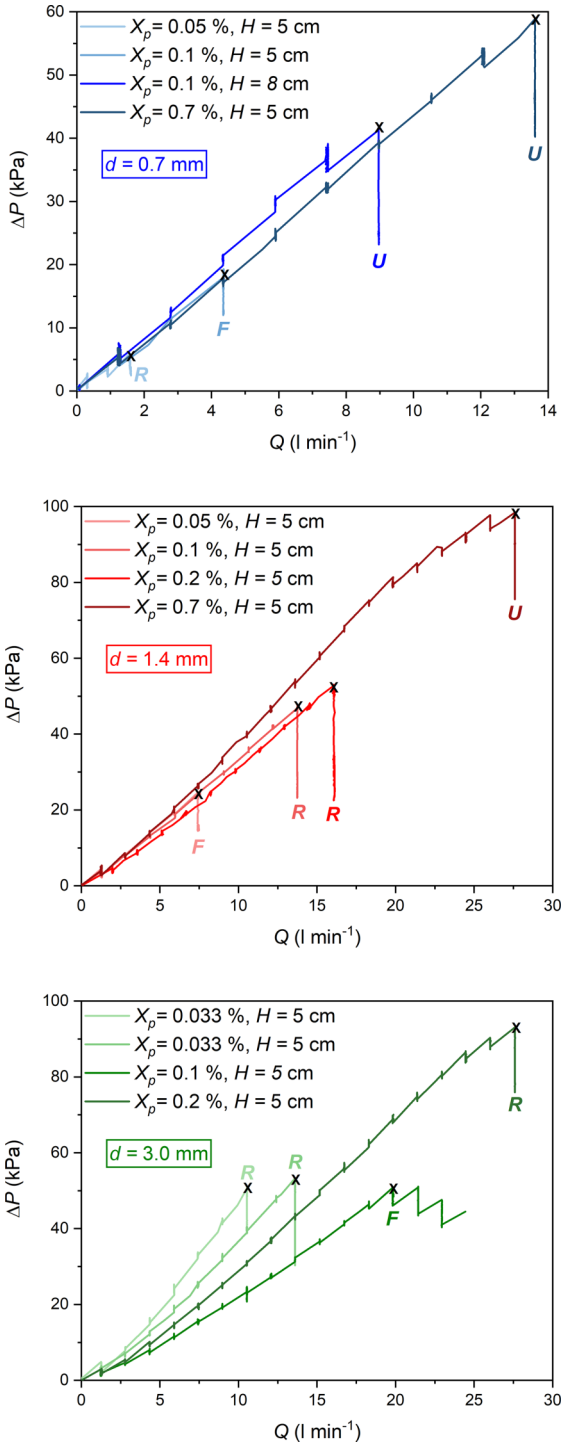

FIG. 8. Pressure difference ΔP as a function of flow rate Q for several experiments on samples with diameter, (a) $d = 0.7$ mm, (b) $d = 1.4$ mm, and (c) $d = 3.0$ mm, with various paraffin contents (from $X_p = 0.033$ to 0.7%) and two bed heights ($H = 5$ and 8 cm). The critical flow rate Q_c and the critical hydraulic pressure difference ΔP_c are indicated by the crosses.

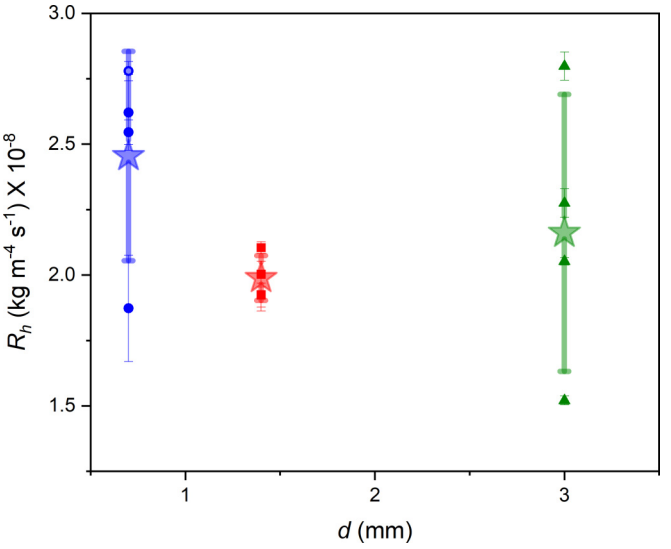

FIG. 9. Hydraulic resistance R_h for the different bead diameters. Each point corresponds to a trial with a solid symbol for $H = 5$ cm and a hollow symbol for $H = 8$ cm. For each bead size, the mean (hollow stars) is plotted with the corresponding standard deviation as error bar.

Knowing that the permeability k of a monosize sphere medium is proportional to the square of their diameter [36], one could have expected a ratio in the order of 20 between minimal and maximal hydraulic resistance. However, this reasoning is true only for uniform flows, which is not the case here due to the localized injection at the base of the porous layer. The lateral extension of the flow is therefore a very important parameter: the more pronounced it is, the more the fluid velocity will be slowed down by mass conservation. A lower permeability favors this lateral extension and, in our specific configuration, reduces the hydraulic resistance. The two extreme cases, corresponding either to zero lateral extension or rapid flow invasion of the entire sample, can be modeled by a uniform porous flow of cross section $S_i = \frac{\pi}{4} D_i^2$ and S_b, respectively. Under uniform Darcy conditions, the hydraulic resistance is simply $R_h = \frac{H}{Sk}$ with S the flow cross section. We can therefore expect a maximum ratio of $\frac{S_b}{S_i} \approx 40$ on the R_h value due to lateral extension. The impact is therefore substantial and could virtually balance almost entirely the influence of the intrinsic permeability.

B. Critical pressure drop

Although each test provides a pair of critical values, i.e., flow rate and pressure difference, the previous discussion shows that it is sufficient to analyze only one of the two quantities, since they are linked by the hydraulic resistance, which remains basically constant during these experiments. We will therefore focus on the variation in critical pressure drop ΔP_c as a function of the sample control parameters. As a first step, Fig. 10 shows ΔP_c values as a function of the paraffin content X_p for the three bead sizes tested.

As expected, ΔP_c increases both with X_p and d, but less markedly for the latter. To simultaneously account for these two parameters consistently, it makes sense to use the microscopic cementation force F_t instead, as presented in Fig. 11.

Although a slight narrowing of the data is achieved, there is still a separation as a function of bead diameter, as well as an upward shift for the $d = 0.7$ mm test performed with a higher sample height ($H = 8$ cm vs $H = 5$ cm). To avoid these geometrical size effects, it appears more pertinent to employ dimensionless numbers as described in the following section.

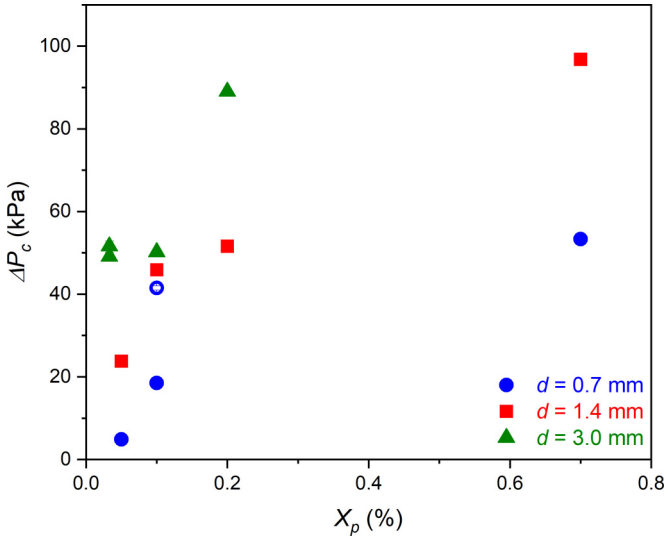

FIG. 10. Critical hydraulic pressure difference ΔP_c as a function of the paraffin mass content X_p for $d = 0.7$ mm (blue circles), $d = 1.4$ mm (red squares), and $d = 3$ mm (green triangles), with bed heights $H = 5$ cm (closed symbols) and $H = 8$ cm (open symbol).

C. Dimensionless scaling

1. Unsuccessful use of the granular Bond number

Naturally, the cohesive granular Bond number Bo_g introduced previously in Eq. (2) appears to be a good candidate for characterizing the strength of a sample. In terms of hydrodynamic forces at the failure trigger, either the critical inlet Reynolds number Re_{i_c} can be used directly, or the

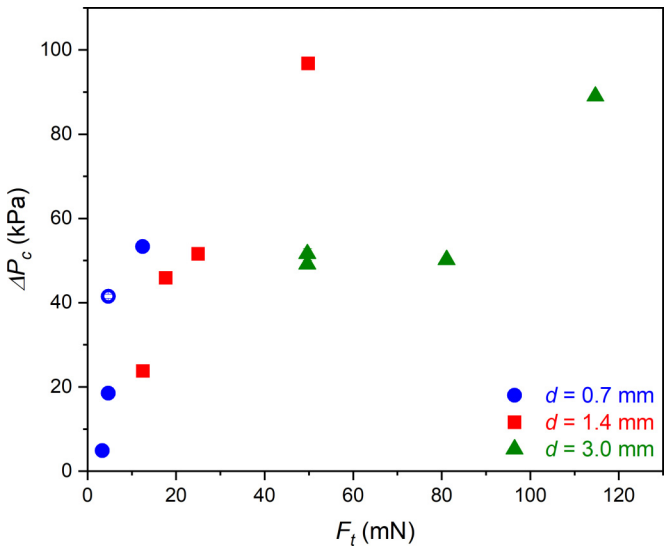

FIG. 11. Critical hydraulic pressure difference ΔP_c as a function of the microscopic cementation force F_t for $d = 0.7$ mm (blue circles), $d = 1.4$ mm (red squares), and $d = 3$ mm (green triangles), with bed heights $H = 5$ cm (closed symbols) and $H = 8$ cm (open symbol).

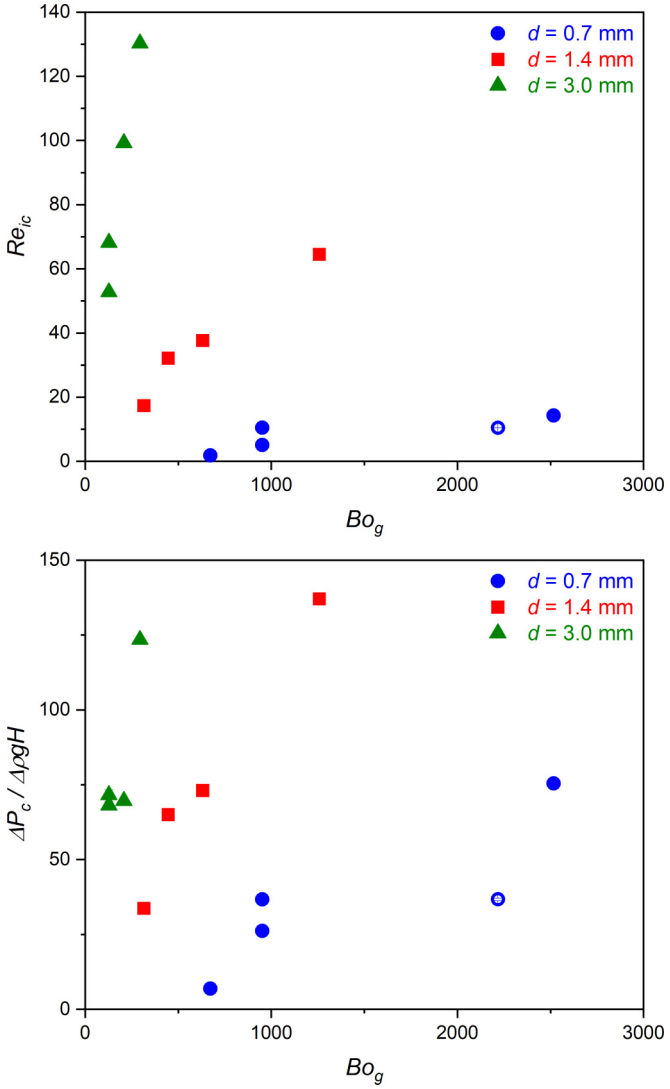

FIG. 12. Critical values of both the inlet porous Reynolds number Re_{i_c} and the dimensionless pressure difference $\frac{\Delta P_c}{\Delta \rho g H}$ as a function of the cohesive granular Bond number Bo_g for $d = 0.7$ mm (blue circles), $d = 1.4$ mm (red squares), and $d = 3$ mm (green triangles), with bed heights $H = 5$ cm (closed symbols) and $H = 8$ cm (open symbol).

differential pressure ΔP_c can be scaled by the gravitational stress associated to the buoyant weight of the sample, namely, $\Delta \rho g H$ with $\Delta \rho = \rho_g - \rho_l$. The corresponding data are displayed in Fig. 12. However, these dimensionless magnitudes do not lead yet to a merging of the experimental data at all, but quite the contrary. Only the gap induced by difference in sample height H seems to be corrected here.

2. Extension of the Archimedes number

In order to rationalize the data in a more meaningful way, one solution is to consider the existing results for the same hydrodynamic configuration, but in the purely frictional case and then to extend them to the cemented case.

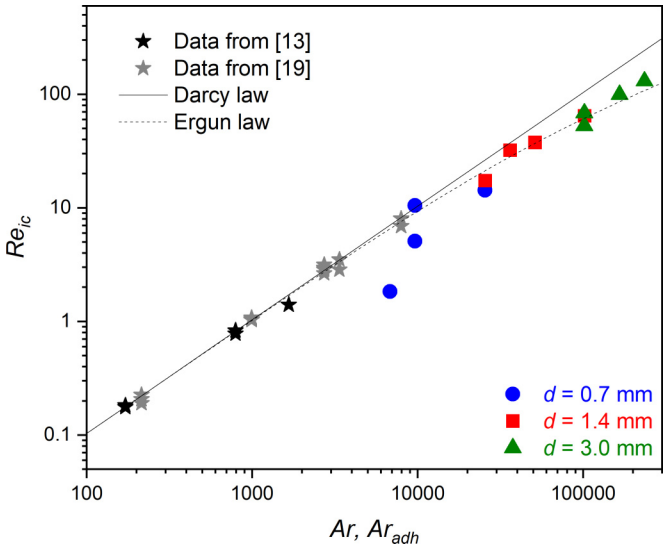

FIG. 13. Critical values of the inlet porous Reynolds number Re_{i_c} as a function of the adhesive Archimedes number $\mathrm{Ar}_{\mathrm{adh}}$ plotted in log-log scale. Previous experimental data from [13] (black stars) and from [19] (gray stars) have been added, based on Ar instead of $\mathrm{Ar}_{\mathrm{adh}}$. The two lines stand for the Darcy (solid line) and Ergun (dotted line) laws.

Thus, as detailed in [19], the set of trigger conditions for localized granular fluidization can be properly grouped together in a diagram representing the critical values of the porous Reynolds number at inlet Re_{i_c} as a function of the Archimedes number Ar, which characterizes the motion of a body in a fluid, due to their difference in density. This number corresponds to the ratio between gravitational forces, inertial forces and viscous forces, and is written as

$$\mathrm{Ar} = \frac{\rho_l \Delta\rho \Omega g}{\mu_l^2}, \tag{4}$$

with Ω the volume of the solid body.

In our cemented materials, the adhesive force between the bonded grains is far greater than the buoyant weight of the particles, which may thus be neglected as evidenced by the range of Bo_g values in Fig. 12. In this way, the buoyant weight $\Delta\rho\Omega g$ can therefore be replaced by the cementation force F_t in the expression of Ar, since both play a broadly similar role in resisting the fluidization of the grains by the upward flow. The definition of this adhesive Archimedes number $\mathrm{Ar}_{\mathrm{adh}}$ is consequently

$$\mathrm{Ar}_{\mathrm{adh}} = \frac{\rho_l F_t}{\mu_l^2}, \tag{5}$$

Note that this number is simply a combination of Ar and Bo_g numbers since $\mathrm{Ar}_{\mathrm{adh}} \propto \mathrm{ArBo}_g$.

The critical values of the inlet porous Reynolds number Re_{i_c} as a function of this adhesive Archimedes number $\mathrm{Ar}_{\mathrm{adh}}$ are summarized in Fig. 13.

Interestingly, all the data are now convincingly gathered on a common trend line. Some data points in the series with $d = 0.7$ mm may deviate slightly, but this can be due to the fact that this small grain size is outside the range for which the semianalytical law for the cementation force in Eq. (1) has been obtained, i.e., for d between 1.4 and 7 mm. Nevertheless this global trend validates the relevance of the adhesive Archimedes number, which directly controls the critical condition for the onset of hydraulic failure of the cemented sample. The high quality of this data collapse is also remarkable given that the failure modes are varied, remaining unpredictable with respect to

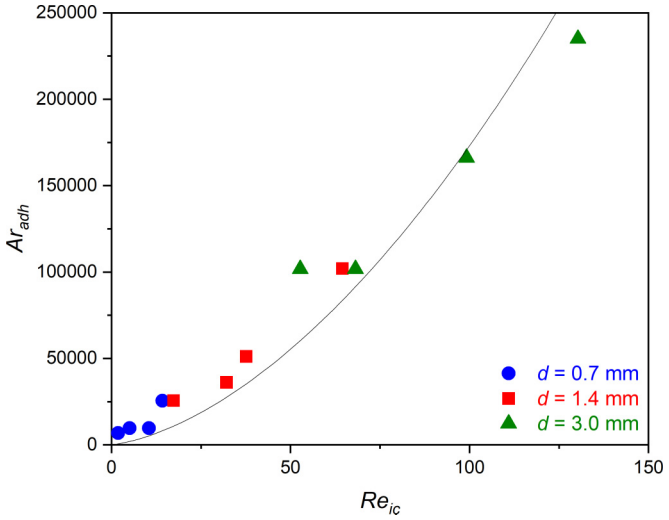

FIG. 14. Plot of the adhesive Archimedes number $\mathrm{Ar}_{\mathrm{adh}}$ as a function of the critical inlet porous Reynolds number Re_{i_c} in linear scales. The line stands for Eq. (6) with $\alpha = 0.15$.

each other, and also very different from the fluidization chimney observed in the purely frictional samples [13,17,19,21].

The data available concerning the localized fluidization onset [13,19] are also included in Fig. 13 for a further comparison between the frictional and cemented cases. In those studies, the same definition of the porous Reynolds number at injection Re_i was used, but, in contrast to the present analysis, the volume of a grain Ω was simply represented dimensionally by d^3 in the expression of Ar, thus omitting the $\frac{\pi}{6}$ prefactor. The latter has therefore been included here for a better quantitative comparison of the data. The cemented data are in this case almost perfectly aligned with those obtained in the frictional case, which can be highlighted once again given the differences in the hydraulic fracture mechanisms. These new values correspond to higher Reynolds numbers and, as expected, gradually deviate from the analytical prediction based on Darcy's law while Ergun's relation remains very well adapted.

All in all, this experimental campaign shows that the dimensionless numbers relevant to understanding granular fluidization remain, rather unexpectedly, those capable of rationalizing the critical conditions for hydraulic failure of a cemented granular material, namely, by the mere introduction of the adhesive Archimedes number.

3. Local scale interpretation

At the scale of cemented particles, it is interesting to determine the force generated by the flow on the granular medium. The order of magnitude of this force corresponds to the drag exerted on a grain and is written as $F_d = \frac{1}{2}\rho_l C_d \frac{\pi d^2}{4} u_l^2$, with C_d the drag coefficient and u_l the relative velocity between the liquid and the grain (which coincides here with the liquid velocity prior destabilization). Around the flow inlet, the mean liquid velocity is $u_l = \frac{4Q}{\pi D_i^2 (1-\phi)}$ and the drag coefficient is thus expressed as a function of the internal porous Reynolds number $\mathrm{Re}_p = \frac{\rho_l u_l d}{\mu_l}$ that differs from the previous inlet Reynolds number Re_i by a factor $(1-\phi)^{-1}$. While several empirical formulas exist, for practical purposes we will adopt the one by Dallavalle given in [37], which can be written as $C_d = (\sqrt{0.44} + \sqrt{\frac{24}{\mathrm{Re}_p}})^2$.

Considering that the drag force is the cause of cemented bond detachment means that F_d must be of the same order of magnitude as the yield tensile force F_t, i.e., $F_d = \alpha F_t$ with α of order 1. It

follows that

$$\mathrm{Ar}_{\mathrm{adh}} = \frac{3\pi}{\alpha}\frac{\mathrm{Re}_{i_c}}{1-\phi}\left(\sqrt{\frac{0.44\mathrm{Re}_{i_c}}{24(1-\phi)}}+1\right)^2. \tag{6}$$

Introducing the volume fraction estimated in our experiments, $\phi = 0.61$, this critical bond failure condition at local grain scale is tested in Fig. 14, and a correct agreement with the data is obtained for $\alpha \approx 0.15$.

Note that the α value may be a little lower than expected, but there are several reasons for this. First, the paraffin bonds are more likely detached by shear rather than tension, and, as already mentioned, this reduces the critical force required by a factor about 0.4. However, there are more bridges to consider per grain. Second, the local velocity of the flow can be significantly increased compared with the mean value used here, particularly when passing through constrictions between pores.

In summary, this analysis shows that, irrespective of its subsequent development, during which boundary conditions obviously play a major role, the initiation of the instability appears to take place very locally at the inlet when the drag force induced by the flow overcomes the adhesive strength of the paraffin bonds.

V. CONCLUSION

This contribution investigated experimentally the failure of artificial soil layers made of cemented granular materials under the hydraulic load generated by an upward flow injected through a small section at the bottom of the system. The paper has focused on the description of the different failure mechanisms observed, the quantification of the critical conditions for their occurrence, and a parametric analysis including the introduction of relevant dimensionless numbers. The major outcomes of the study can be summarized as follows:

(i) Concerning the failure phenomenology, the initial tests showed that the main mode of hydraulic failure of the cemented samples is the block uplift caused by their complete detachment from the cell walls, with no other apparent damage to the samples. This mechanism, related to the specific weakness of the cemented samples at the boundaries, could be partially inhibited by reinforcing the paraffin bridges at the walls with a prior coating. Two other failure scenarios were then observed, one consisting of a two-block fracturing of the sample at the flow inlet, and the other corresponding to the progressive burrowing of a flow path by localized fluidization of the sample along the walls.

(ii) The measured critical values for flow rate and pressure difference at failure increase with grain size, cementation strength, and sample thickness as expected, but do not allow a clear discrimination between the different failure modes. The hydraulic resistance of the sample is well defined up to the failure onset and can be directly estimated from the measurements, appearing to be virtually independent of the grain size due to the antagonistic impacts of the intrinsic permeability and lateral flow extension.

(iii) The use of the cohesive granular Bond number alone does not lead to any convincing rationalization of the experimental data. However, it appears pertinent to consider an adhesive form of the Archimedes number, simply by combining the usual Archimedes number and the cohesive granular Bond number so that the buoyant weight is replaced by the tensile strength of the cementation bonds. This magnitude manages to gather the whole experimental data set together and, unexpectedly, in close agreement with the trend curve proposed in the literature for the localized fluidization of a purely frictional material, even though the subsequent physical mechanisms of destabilization are radically different.

(iv) A detailed analysis of the results obtained suggests the following interpretation for understanding the hydraulic fracturing of our artificial cemented granular materials. The onset of instability takes place in the immediate vicinity of the injection nozzle, through the gradual detachment of paraffin bonds, allowing grains to be released and set in motion. This is followed by the

more or less gradual development of a decementation route, probably associated with a preferential flow path. This second phase, from grain to sample scale, is strongly controlled by the boundaries and explains the observation of several failure modes. This global scenario explains why the same initiation threshold is reached regardless of the subsequent progression of the destabilization and final failure morphology.

In summary, this study could pave the way for an extension of the dimensional relationships established for particulate systems interacting with a fluid flow to the case of cemented granular materials, not only in the context of fluidization but also more widely. However, these initial encouraging results would need of course to be confirmed by future studies on the effects of hydraulic loading on cemented granular materials, for instance, following on from this work and other previous investigations on the surface erosion of soils [24,33].

ACKNOWLEDGMENTS

The authors acknowledge financial support by the French National Research Agency for the Franco-German project COMET (Grant No. ANR-2018-CE92-0007). This work benefited from the contribution of Surya Balagani as an internship student. A.F. thanks the UFA-DFH for granting a Franco-German joint Ph.D. scholarship.

[1] B. D. Collins and N. Sitar, Stability of steep slopes in cemented sands, J. Geotech. Geoenviron. Eng. **137**, 43 (2011).

[2] A. Tengattini, E. Andò, I. Einav, and G. Viggiani, Micromechanically inspired investigation of cemented granular materials: Part I—From x-ray micro tomography to measurable model variables, Acta Geotech. **18**, 57 (2023).

[3] D. Terzis and L. Laloui, A decade of progress and turning points in the understanding of bio-improved soils: A review, Geomech. Energy Environ. **19**, 100116 (2019).

[4] M. Sarkis, A. Naillon, F. Emeriault, and C. Geindreau, Tensile strength measurement of the calcite bond between biocemented sand grains, Acta Geotech. **19**, 1555 (2023).

[5] W. Powrie, *Soil Mechanics: Concepts and Applications*, 2nd ed. (CRC Press, New York, 2004).

[6] H. Mikulčić, J. J. Klemeš, M. Vujanović, K. Urbaniec, and N. Duić, Reducing greenhouse gasses emissions by fostering the deployment of alternative raw materials and energy sources in the cleaner cement manufacturing process, J. Cleaner Prod. **136**, 119 (2016).

[7] H. Kou, H. Jing, C. Wu, P. Ni, Y. Wang, and S. Horpibulsuk, Microstructural and mechanical properties of marine clay cemented with industrial waste residue-based binder (IWRB), Acta Geotech. **17**, 1859 (2022).

[8] A. Schmeink, L. Goehring, and A. Hemmerle, Fracture of a model cohesive granular material, Soft Matter **13**, 1040 (2017).

[9] S. F. V. Marques, L. Festugato, and N. C. Consoli, Stiffness and strength of an artificially cemented sand cured under stress, Granular Matter **23**, 35 (2021).

[10] S. Bonelli, *Erosion in Geomechanics Applied to Dams and Levees* (Wiley-ISTE, New York, 2013).

[11] V. M. van Beek, H. Knoeff, and H. Sellmeijer, Observations on the process of backward erosion piping in small-, medium- and full-scale experiments, Eur. J. Environ. Civ. Eng. **15**, 1115 (2011).

[12] V. M. van Beek, H. M. van Essen, K. Vandenboer, and A. Bezuijen, Developments in modelling of backward erosion piping, Géotechnique **65**, 740 (2015).

[13] P. Philippe and M. Badiane, Localized fluidization in a granular medium, Phys. Rev. E **87**, 042206 (2013).

[14] V. M. van Beek, A. Bezuijen, J. B. Sellmeijer, and F. B. J. Barends, Initiation of backward erosion piping in uniform sands, Géotechnique **64**, 927 (2014).

[15] S. Akrami, A. Bezuijen, V. van Beek, E. Rosenbrand, J. Terwindt, and U. Förster, Analysis of development and depth of backward erosion pipes in the presence of a coarse sand barrier, Acta Geotech. **16**, 381 (2021).
[16] E. Rosenbrand, V. van Beek, A. Bezuijen, S. Akrami, J. Terwindt, A. Koelewijn, and U. Forster, Multi-scale experiments for a coarse sand barrier against backward erosion piping, Géotechnique **72**, 216 (2022).
[17] F. Zoueshtiagh and A. Merlen, Effect of a vertically flowing water jet underneath a granular bed, Phys. Rev. E **75**, 056313 (2007).
[18] X. Cui, J. Li, A. Chan, and D. Chapman, Coupled DEM–LBM simulation of internal fluidisation induced by a leaking pipe, Powder Technol. **254**, 299 (2014).
[19] S. E. Mena, L.-H. Luu, P. Cuellar, P. Philippe, and J. S. Curtis, Parameters affecting the localized fluidization in a particle medium, AIChE J. **63**, 1529 (2017).
[20] J. Ngoma, P. Philippe, S. Bonelli, F. Radjai, and J.-Y. Delenne, Two-dimensional numerical simulation of chimney fluidization in a granular medium using a combination of discrete element and lattice Boltzmann methods, Phys. Rev. E **97**, 052902 (2018).
[21] S. E. Mena, F. Brunier-Coulin, J. S. Curtis, and P. Philippe, Experimental observation of two regimes of expansion in localized fluidization of a granular medium, Phys. Rev. E **98**, 042902 (2018).
[22] L.-H. Luu, G. Noury, Z. Benseghier, and P. Philippe, Hydro-mechanical modeling of sinkhole occurrence processes in covered karst terrains during a flood, Eng. Geol. **260**, 105249 (2019).
[23] Z. Benseghier, P. Cuéllar, L.-H. Luu, S. Bonelli, and P. Philippe, A parallel GPU-based computational framework for the micromechanical analysis of geotechnical and erosion problems, Comput. Geotech. **120**, 103404 (2020).
[24] Z. Benseghier, L.-H. Luu, P. Cuéllar, S. Bonelli, and P. Philippe, On the erosion of cohesive granular soils by a submerged jet: A numerical approach, Granular Matter **25**, 8 (2023).
[25] X. Cui, J. Li, A. Chan, and D. Chapman, A 2D DEM–LBM study on soil behaviour due to locally injected fluid, Particuology **10**, 242 (2012).
[26] D. Tran, N. Prime, F. Froiio, C. Callari, and E. Vincens, Numerical modelling of backward front propagation in piping erosion by DEM-LBM coupling, Eur. J. Environ. Civ. Eng. **21**, 960 (2017).
[27] A. Theocharis, J.-N. Roux, and V. Langlois, Elasticity of model weakly cemented granular materials: A numerical study, Int. J. Solids Struct. **193-194**, 13 (2020).
[28] A. Farhat, L.-H. Luu, P. Philippe, and P. Cuellar, Multi-scale cohesion force measurements for cemented granular materials, EPJ Web Conf. **249**, 08008 (2021).
[29] A. Farhat, L.-H. Luu, A. Doghmane, P. Cuellar, N. Benahmed, T. Wichtmann, and P. Philippe, Micro and macro mechanical characterization of artificial cemented granular materials, Granular Matter **26**, 65 (2024).
[30] S. T. Nase, W. L. Vargas, A. A. Abatan, and J. McCarthy, Discrete characterization tools for cohesive granular material, Powder Technol. **116**, 214 (2001).
[31] A. Castellanos, The relationship between attractive interparticle forces and bulk behaviour in dry and uncharged fine powders, Adv. Phys. **54**, 263 (2005).
[32] A. Anand, J. S. Curtis, C. R. Wassgren, B. C. Hancock, and W. R. Kettrehagen, Predicting discharge dynamics of wet cohesive particles from a rectangular hopper using the discrete element method (DEM), Chem. Eng. Sci. **64**, 5268 (2009).
[33] F. Brunier-Coulin, P. Cuellar, and P. Philippe, Generalized shields criterion for weakly cohesive granular materials, Phys. Rev. Fluids **5**, 034308 (2020).
[34] V. Richefeu, M. S. E. Youssoufi, and F. Radjai, Shear strength properties of wet granular materials, Phys. Rev. E **73**, 051304 (2006).
[35] D. Hlushkou and U. Tallarek, Transition from creeping via viscous-inertial to turbulent flow in fixed beds, J. Chromatogr. A **1126**, 70 (2006).
[36] J. Bear, *Dynamics of Fluids in Porous Media*, Dover Civil and Mechanical Engineering Series (Dover, 1988).
[37] R. Di Felice, The voidage function for fluid-particle interaction systems, Int. J. Multiphase Flow **20**, 153 (1994).